HHS Public Access

Author manuscript

Magn Reson Med. Author manuscript; available in PMC 2023 November 01.

Published in final edited form as:

Magn Reson Med. 2023 October ; 90(4): 1502–1517. doi:10.1002/mrm.29742.

Validation of the presence of fast exchanging amine CEST effect at low saturation powers and its influence on the quantification of APT

Casey Sun[1,2], **Yu Zhao**[1,3], **Zhongliang Zu**[1,3,4]

[1]Vanderbilt University Institute of Imaging Science, Vanderbilt University Medical Center, Nashville, US.

[2]Department of Chemistry, University of Florida, Gainesville, US.

[3]Department of Radiology and Radiological Sciences, Vanderbilt University Medical Center, Nashville, US.

[4]Department of Biomedical Engineering, Vanderbilt University, Nashville, US.

Abstract

Purpose: Accurately quantifying the amide proton transfer (APT) effect and the underlying exchange parameters is crucial for its applications, but previous studies have reported conflicting results. In these quantifications, the chemical exchange saturation transfer (CEST) effect from the fast exchange amine was always ignored because it was considered weak with low saturation powers. This paper aims to evaluate the influence of the fast exchange amine CEST on the quantification of APT at low saturation powers.

Methods: A quantification method with low and high saturation powers was used to distinguish APT from the fast exchange amine CEST effect. Simulations were conducted to assess the method's capability to separate APT from the fast exchange amine CEST effect. Animal experiments were performed to assess the relative contributions from the fast exchange amine and amide to CEST signals at 3.5ppm. Three APT quantification methods, each with varying degrees of contamination from the fast exchange amine, were employed to process the animal data to assess the influence of the amine on the quantification of APT effect and the exchange parameters.

Results: The relative size of the fast exchange amine CEST effect to APT effect gradually increases with increasing saturation power. At 9.4T, it increases from approximately 20% to 40% of APT effect with a saturation power increase from 0.25 μT to 1 μT.

Conclusion: The fast exchange amine CEST effect leads overestimation of APT effect, fitted amide concentration, and amide–water exchange rate, potentially contributing to the conflicting results reported in previous studies.

Correspondence to: Zhongliang Zu, Ph.D., Vanderbilt University Institute of Imaging Science, 1161 21st Ave. S, Medical Center North, AAA-3112, Nashville, TN 37232-2310, zhongliang.zu@vumc.org, Phone: 615-875-9815, Fax: 615-322-0734.

Keywords

chemical exchange saturation transfer (CEST); amide proton transfer (APT); amine; quantification

INTRODUCTION

Chemical exchange saturation transfer (CEST) is an MR contrast mechanism used for molecular and pH imaging (1-5). It involves applying a frequency-selective radiofrequency (RF) saturation pulse to exchangeable protons in the solute. The saturated solute protons transfer their magnetization to water protons via chemical exchange. This exchange leads to a detectable change in the water signal, which can be measured to provide enhanced sensitivity. Amide proton transfer (APT) is a common application of CEST imaging that detects mobile proteins/peptides at approximately 3.5ppm from water. It is also sensitive to pH variation at relatively low saturation powers (6). APT imaging has been used to detect malignant brain tumors with the assumption that it can measure overexpressed proteins (thus, increasing protein amide concentration) in tissues with increased cell density (7-10). Additionally, APT imaging has been applied to detect ischemic stroke because of tissue acidosis (thus, a decreased amide–water exchange rate) (11-13).

Accurate quantification of the APT effect, amide concentration, or amide–water exchange rate is crucial for protein and pH imaging. However, different quantification results have been reported previously (e.g., the fitted amide–water exchange rates range from dozens of s^{-1} to a few hundreds of s^{-1} in previous studies (6,14,15)), and the underlying reason is unknown. CEST peaks, especially those from exchangeable protons in the fast exchange regime, are broad compared with their frequency offsets from water, which may introduce errors in their quantifications. In the nervous system, there is a fast exchange amine pool from glutamate and proteins at approximately 3ppm (16,17), which is very close to the amide frequency offset of 3.5ppm and should have overlapping CEST signals with APT. In previous quantification of the APT effect with relatively low saturation powers, the contribution from the fast exchange amine to the CEST signal at 3.5ppm was always ignored based on the fact that the fast exchange protons cannot be effectively saturated at low saturation powers. However, this has not been validated.

Besides the APT at 3.5ppm and the fast exchanging amine CEST at 3ppm, there is a guanidinium proton CEST effect at 2ppm, primarily from creatine (18,19). Although the APT and guanidinium proton CEST peaks are relatively narrow compared with the fast exchange amine CEST peak, the overlapping of these two narrow CEST peaks creates a broad baseline, making it difficult to identify the broad CEST peak from the fast exchange amine and thus difficult to accurately separate the APT effect from the fast exchange amine CEST effect based on their different peak shapes. Previously, we developed a quantification method using low and high saturation power to distinguish CEST effects from slow and fast exchange pools. Using this method, we estimated the relative size of the fast exchange amine to APT (i.e., fast exchange amine CEST/APT) at 1μT (20). In this paper, we applied this quantification method to estimate the relative size of the fast exchange amine to APT at two additional saturation powers of 0.25μT and 0.5μT, allowing us to observe the trend

of CEST effects from these two pools with increasing saturation power. Additionally, we conducted simulations and experiments both with and without the incorporation of the fast exchange amine CEST effect to evaluate its impact on the quantification of the APT effect and underlying exchange parameters.

THEORY

In a multiple-pool model including direct water saturation (DS), semi–solid magnetization transfer (MT), and CEST effects in the slow (s) and fast (f) exchange regimes, these effects acquired in steady state can be described simultaneously by superimposing their rotating frame relaxations (when the concentrations of CEST and MT pools are much less than 1) (21,22),

$$R_{1\rho}(\Delta\omega) \approx R_{eff}(\Delta\omega) + \frac{R_{ex}^{s}(\Delta\omega)}{1+f_m} + \frac{R_{ex}^{f}(\Delta\omega)}{1+f_m} + R_{ex}^{MT}(\Delta\omega) \quad (1)$$

where $R_{1\rho}$, R_{ex} (R_{ex}^{s}, R_{ex}^{f}) and R_{ex}^{MT} are the water longitudinal relaxation in the rotating frame, CEST effect from the slow exchange pool and fast exchange pool in the rotating frame, and semi-solid MT effect in the rotating frame respectively; R_{eff} is the water relaxation; Δω is the RF frequency offset; and f_m is the semi–solid component concentration. $R_{1\rho}$, R_{ex}^{s}, and R_{ex}^{f} can be described by (23)

$$R_{1\rho}(\Delta\omega) \approx \frac{S_0 R_{1obs}}{S(\Delta\omega)} \quad (2)$$

$$R_{ex}^{s}(\Delta\omega) = \frac{f_s^s k_{sw}^s \omega_1^2}{\omega_1^2 + (R_{2s}^s + k_{sw}^s)k_{sw}^s + (\Delta\omega - \Delta^s)^2 k_{sw}^s / (R_{2s}^s + k_{sw}^s)} \quad (3)$$

$$R_{ex}^{f}(\Delta\omega) = \frac{\Delta^{f2}}{\omega_1^2 + \Delta\omega^2} \frac{f_s^f k_{sw}^f \omega_1^2}{\omega_1^2 + (R_{2s}^f + k_{sw}^f)k_{sw}^f + (\Delta\omega - \Delta^f)^2 k_{sw}^f / (R_{2s}^f + k_{sw}^f)} \quad (4)$$

where S is the CEST signal; S_0 is the control signal with no saturation pulses; R_{1obs} is the observed water longitudinal relaxation rate; ω_1 is the saturation power; k_{sw} is the solute–water exchange rate; Δ is the solute frequency offset; and R_{2s} is the solute transverse relaxation rate.

In CEST imaging, a low ω_1 value (around or less than 1μT) is typically used to fit the slow–exchange amide–water exchange effect and to obtain a CEST Z-spectrum in which APT and other CEST peaks can be easily resolved (24). A high ω_1 (e.g., >3.6μT) is used to detect the fast exchange amine CEST effect (25). For the fast exchange pool, k_{sw} (e.g. 5000s^{-1} (25)) is much higher than the low ω_1 (e.g. 268rad·s^{-1} for ω_1 of 1μT) or the high ω_1 (e.g. 964rad·s^{-1} for ω_1 of 3.6μT). Additionally, at 3.5ppm, Δω (i.e., 2815rad/s and 8797rad/s at 3T and 9.4T, respectively) is much higher than the low and the high ω_1. Thus, ω_1 in the denominator of both the first and the second term in Eq. (4) can be ignored. The total contribution from

both the slow and the fast exchange pools ($R_{ex}^{s+f} = R_{ex}^{s} + R_{ex}^{f}$) with normalization of ω_1^2 at low saturation powers ω_{1_l} can then be described by

$$\frac{R_{ex}^{s+f}(\Delta\omega)\mid_{low\,\omega_1}}{\omega_{1\_l}^2} = \frac{f_s^s k_{sw}^s}{\omega_{1\_l}^2 + (R_{2s}^s + k_{sw}^s)k_{sw}^s + (\Delta\omega - \Delta^s)^2 k_{sw}^s / (R_{2s}^s + k_{sw}^s)} + \frac{\Delta^{f2}}{\Delta\omega^2}\frac{f_s^f k_{sw}^f}{(R_{2s}^f + k_{sw}^f)k_{sw}^f + (\Delta\omega - \Delta^f)^2 k_{sw}^f / (R_{2s}^f + k_{sw}^f)} \tag{5}$$

At high saturation powers (ω_{1_h}), it can be described by

$$\frac{R_{ex}^{s+f}(\Delta\omega)\mid_{high\,\omega_1}}{\omega_{1\_h}^2} = \frac{f_s^s k_{sw}^s}{\omega_{1\_h}^2 + (R_{2s}^s + k_{sw}^s)k_{sw}^s + (\Delta\omega - \Delta^s)^2 k_{sw}^s / (R_{2s}^s + k_{sw}^s)} + \frac{\Delta^{f2}}{\Delta\omega^2}\frac{f_s^f k_{sw}^f}{(R_{2s}^f + k_{sw}^f)k_{sw}^f + (\Delta\omega - \Delta^f)^2 k_{sw}^f / (R_{2s}^f + k_{sw}^f)} \tag{6}$$

Note that R_{ex}^f / ω_1^2 (the second term in Eq. (5) and Eq. (6)) is independent of ω_1. Thus, subtracting two R_{ex}^{s+f} acquired at a low ω_1 (i.e., Eq. (5)) and at a high ω_1 (i.e. Eq. (6)) can remove the contribution from the fast exchange CEST effects (i.e., R_{ex}^f). For the slow exchange pool, k_{sw} (e.g., $100s^{-1}$) is comparable to the low ω_1 (e.g., $67rad{\cdot}s^{-1}$, $134rad{\cdot}s^{-1}$, and $268rad{\cdot}s^{-1}$ for ω_1 of 0.25μT, 0.5μT, and 1μT, respectively) and much lower than the high ω_1 (e.g., $964rad{\cdot}s^{-1}$ for ω_1 of 3.6μT). Thus, R_{ex}^s / ω_1^2 acquired at a high ω_1 (the first term in Eq. (6)) is a few times lower than that acquired at a low ω_1 (the first term in Eq. (5)). R_{ex}^s / ω_1^2 acquired at a low ω_1 (the first term in Eq. (5)) can be ignored when subtracting Eq. (5) from Eq. (6). Then,

$$\frac{R_{ex}^{s+f}(\Delta\omega)\mid_{low\,\omega_1}}{\omega_{1\_l}^2} - \frac{R_{ex}^{s+f}(\Delta\omega)\mid_{high\,\omega_1}}{\omega_{1\_h}^2} = \frac{f_s^s k_{sw}^s}{\omega_{1\_l}^2 + (R_{2s}^s + k_{sw}^s)k_{sw}^s + \frac{(\Delta\omega - \Delta^s)^2 k_{sw}^s}{R_{2s}^s + k_{sw}^s}} = \frac{R_{ex}^s(\Delta\omega)\mid_{low\,\omega_1}}{\omega_{1\_l}^2} \tag{7}$$

Thus, a rough estimation of R_{ex}^s and R_{ex}^f at a low ω_1 can be obtained by R_{ex}^{s+f} acquired at a high and low ω_1,

$$R_{ex}^s(\Delta\omega)\mid_{low\,\omega_1} \approx \left(\frac{R_{ex}^{s+f}(\Delta\omega)\mid_{low\,\omega_1}}{\omega_{1\_l}^2} - \frac{R_{ex}^{s+f}(\Delta\omega)\mid_{high\,\omega_1}}{\omega_{1\_h}^2}\right)\omega_{1\_l}^2 \tag{8}$$

$$R_{ex}^f(\Delta\omega)\mid_{low\,\omega_1} \approx \frac{R_{ex}^{s+f}(\Delta\omega)\mid_{high\,\omega_1}}{\omega_{1\_h}^2}\omega_{1\_l}^2 \tag{9}$$

Based on Eq. (2), R_{ex} can be quantified by an inverse subtraction of the label signal ($S_{lab}(\Delta\omega)$) and reference signal ($S_{ref}(\Delta\omega)$) together with $T_{1obs}(1 / R_{1obs})$ normalization, known as apparent exchange-dependent relaxation (AREX) (21,22,26),

$$AREX(\Delta\omega) = \left(\frac{S_0}{S_{lab}(\Delta\omega)} - \frac{S_0}{S_{ref}(\Delta\omega)}\right)R_{1obs}(1 + f_m) = R_{ex} \quad (10)$$

where the label signal contains contributions from the CEST effect and other nonspecific background signals (e.g., DS and MT). The reference signal contains contributions from only the nonspecific background signals, which can be obtained by fitting CEST data acquired beyond the frequency range of CEST effects (24,27).

METHODS

Animal Preparation

Five healthy rats were included to evaluate the relative contribution of the fast exchange amine CEST and APT to the CEST signal at 3.5ppm. Eight rats bearing 9L tumors were included to evaluate the impact of the fast exchange amine CEST effect on the APT effect. Tumor induction involved injecting 1×10^5 9L glioblastoma cells into the right brain hemisphere, followed by imaging after 2 to 3 weeks. All rats were immobilized and anesthetized with 2–3% isoflurane and 97–98% oxygen for both induction and maintenance during the experiments, ensuring a respiration rate of 40-70 breaths per minute. The rectal temperature was maintained at 37°C using a warm-air feedback system. All animal procedures were approved by the Animal Care and Usage Committee of Vanderbilt University.

MRI

CEST measurements were performed by applying a continuous wave (CW)–CEST sequence with a 5s rectangular RF saturation pulse followed by single–shot spin–echo echo planar imaging (SE–EPI) acquisition. CEST images were acquired with a ω_1 of 0.25μT, 0.5μT, 1μT and 3.6μT. CEST Z–spectra with ω_1 of 0.25μT, 0.5μT, and 1μT were acquired with Δω from −4000Hz to −2500Hz with a step size of 500Hz (−10ppm to −6.25ppm at 9.4T), −2000Hz to 2000Hz with a step size of 50 Hz (−5ppm to 5ppm at 9.4T), and 2500Hz to 4000Hz with a step size of 500 Hz (6.25ppm to 10ppm at 9.4T). CEST Z–spectra with a ω_1 of 3.6μT were acquired with Δω from −6500Hz to −3500Hz with a step size of 500 Hz (−16.25ppm to −8.75ppm at 9.4T), −2000Hz to 2000Hz with steps of 50Hz (−5ppm to 5ppm at 9.4T), and 3500Hz to 6500Hz with a step size of 500Hz (8.75ppm to 16.25ppm at 9.4T). Control images were acquired with an Δω of 100,000Hz (250ppm at 9.4T). R_{1obs} and f_m were obtained using a selective inversion recovery (SIR) quantitative MT method (28). All measurements were performed on a Varian DirectDrive™ horizontal 9.4T magnet with a 38mm Litz RF coil (Doty Scientific Inc. Columbia, SC) with matrix size 64×64, field of view 30×30 mm^2, and one acquisition.

Data analysis

To assess the relative contribution of the APT and the fast exchanging amine CEST effects, an extrapolated semi–solid MT reference (EMR) approach (29-31) was used to obtain the reference signal for quantifying all CEST effects. The EMR method has been previously used to process CEST Z-spectra acquired at relatively high saturation powers (i.e., 3.6μT) (20) and is therefore suitable for use in this study. Specifically, CEST Z–spectra with a $\Delta\Omega$ from −6500Hz to −3500Hz and 3500Hz to 6500Hz and a ω_1 of 3.6μT, and with a $\Delta\omega$ from −4000Hz to −2500Hz and 2500Hz to 4000Hz and a ω_1 of 1.0μT were fitted to a two-pool MT model (20). The MT parameters including the coupling rate between the semi–solid component and water (k_{mw}), transverse relaxation time of the semi-solid component (T_{2m}), $k_{mw}f_mT_{1w}$, and frequency offset of the semi-solid component (Δ_m) were fitted, and the reference signals in an offset range from −5 ppm to 5 ppm were then estimated using the fitted parameters. The ratio of water longitudinal relaxation time and water transverse relaxation time (T_{1w} / T_{2w}) was set to be 45 for the animal study by literature survey (32). The MT absorption line shape was assumed to be a Lorentzian function. R_{ex_EMR} can then be obtained by Eq. (10).

To evaluate the influence of the fast exchanging amine CEST effect on the quantification of the APT effect and the underlying exchange parameters, we employed three different multiple-pool Lorentzian fit methods (mfit). These include the six–pool Lorentzian fit of the APT effect (mfit_6pool_APT), the two-pool Lorentzian fit of all CEST effect (mfit_2pool_CEST), and the six-pool Lorentzian fit with inclusion of all CEST effects (mfit_6pool_CEST). It should be noted that the APT effect was quantified using all three methods. The model function of the multiple–pool Lorentzian fit method is shown in Eq. (11)

$$\frac{S(\Delta\omega)}{S_0} = 1 - \sum_{i=1}^{N} L_i(\Delta\omega) \tag{11}$$

Here, $L_i(\Delta\omega) = A_i / (1 + (\Delta\omega-\Delta_i)^2 / (0.5W_i)^2)$, which represents a Lorentzian line with a central frequency offset from water (Δ_i), peak full width at half maximum (W_i), and peak amplitude (A_i). The six-pool model contains amide at 3.5ppm, guanidinium proton at 2ppm, water, nuclear Overhauser enhancement (NOE) at −1.6ppm (33-38) and −3.5ppm (27,39,40), and semi–solid MT (41,42). The S_{ref} for the six–pool model fitted APT was obtained by summing all Lorentzians except the amide pool (43). The two–pool model contains water and semi–solid MT pool. The S_{ref} for the two-pool model fitting was obtained by processing the CEST Z–spectrum with frequency offsets of ±4000, ±3500, ±3000, ±2500, ±200, ±150, ±100, ±50, and 0Hz (−10 to −6.25ppm, −0.5 to 0.5ppm, and 6.25 to 10ppm at 9.4T). The six–pool model fit with inclusion of all CEST effects is based on the fitted components of the six-pool model. S_{ref} for the six–pool model fit with inclusion of all CEST effects was obtained by the sum of the water and semi–solid MT pools fitted from the above six-pool model fit. Table 1 lists the starting points and boundaries of the multiple–pool Lorentzian fit. The goodness of the fit was estimated with the averaged root mean square (RMS) of residuals across the frequency range of the z-spectrum used for the fitting. R_{ex} spectra quantified from

the above three quantification methods, termed $R_{ex\_mfit\_6pool\_APT}$, $R_{ex\_mfit\_2pool\_CEST}$, and $R_{ex\_mfit\_6pool\_CEST}$ were obtained using Eq. (10). Previously, we have shown that the six-pool model Lorentzian fit is capable of accurately quantifying the APT effect when ω_1 is equal to or less than 1μT at 9.4T (24). Thus $R_{ex\_mfit\_6pool\_APT}$ should have minimal to no contribution from the fast exchange amine. S_{ref} for the six–pool model with inclusion of all CEST effects should only include contributions from water and MT effects, resulting in $R_{ex\_mfit\_6pool\_CEST}$ containing all CEST effects but no water and MT effects. At 3.5ppm, $R_{ex\_mfit\_6pool\_CEST}$ at 3.5ppm should have the maximum contribution from the fast exchange amine CEST effect. on the other hand, the two–pool model Lorentzian fit processes CEST signals with RF frequency not only beyond ±6.25ppm but also between −0.5ppm and 0.5ppm, where there are significant contributions from the fast exchange pools due to their coalesce effects with water. Therefore, S_{ref} for the two-pool model Lorentzian fit should have contributions from water, MT, and a part of the fast exchange amine CEST effect. As a result, $R_{ex\_mfit\_2pool\_CEST}$ should contain some contribution from the fast exchange amine. It is important to note that although the EMR method also fits water and MT effects, it does not process CEST signals near to water line, resulting in minimal to no contamination from the fast exchange amine. These three quantification models have varying degrees of contamination from the fast exchange amine to CEST signals at 3.5ppm, providing a useful framework for evaluating the influence of the fast exchange amine CEST effect on the quantification of amide–water exchange parameters.

The R_{ex} values at 3.5ppm with the three ω_1 values were fitted to Eq. (3) to obtain the amide f_s and amide k_{sw}. In animal studies, the T_{2s} value was set to three different values (5ms, 2ms, and 1.5ms) during the fitting process since it can influence the quantification of f_s and k_{sw}.

Regions of interest (ROIs) were drawn from the whole brain in the healthy rat brains and were drawn from the tumor region and the contralateral normal tissues in the rat brains bearing tumors. Student's t test was employed to evaluate the difference in R_{ex} values between tumors and contralateral normal tissues. Differences were considered to be statistically significant when $P < 0.05$.

Numerical simulations

A two–pool (either amide + water or amine + water) model and a three–pool (amide + amine + water) model numerical simulation of coupled Bloch equations were performed with a CW-CEST sequence with a 5s saturation. The amide and amine pools represented the slow and fast exchange pools, respectively. To quantify the R_{ex}^{s} spectrum in the two–pool (amide + water) model simulation and the R_{ex}^{f} spectrum in the two–pool (amine + water) model simulation, and the R_{ex}^{s+f} spectrum in the three-pool model simulations, a reference spectrum was obtained by nulling all exchangeable pools in the simulations (i.e., a single water pool model). The R_{ex} spectrum or R_{ex} value at 3.5ppm was then calculated using the AREX metric defined in Eq. (10). Table 2 lists the simulation parameters.

1. To verify the dependence of R_{ex}^{s} / ω_1^2 on ω_1 and the independence of R_{ex}^{f} / ω_1^2 on ω_1, we performed simulations using a two-pool model (amide + water for the slow exchange pool,

amine + water for the fast exchange pool). The simulations were conducted with ω_1 values varying from 0.2μT to 5μT with a step of 0.2μT.

2. To assess the capability of our quantification method in isolating the slow exchange pool from the fast exchange pool using low and high power, we simulated CEST Z-spectra using the two–pool model with low ω_1 values of 0.25μT, 0.5μT, and 1μT and the three–pool model with low ω_1 values of 0.25μT, 0.5 μT, and 1μT and a high ω_1 value of 3.6μT. Δω was varied from −2000 Hz to 2000 Hz with steps of 50 Hz. The R_{ex}^{s} and R_{ex}^{f} spectra were obtained from the three–pool model simulations using Eq. (8) and Eq. (9), respectively, with ω_1 values of 0.25μT, 0.5μT, 1μT and 3.6μT, and were compared with those obtained from the two–pool model simulations with a ω_1 of 0.25μT, 0.5 μT, and 1μT.

3. To assess how the presence of the fast exchange amine influences the quantification of amide-water exchange parameters, we performed a three–pool model simulation with the amine f_s increased from 0% to 1% with a step of 0.2%, using ω_1 values of 0.25μT, 0.5μT, and 1μT. The simulated CEST signals were generated with noises (S_n) using the randn function in MATLAB to reach a signal–to–noise ratio (SNR) of 500 by $((S + S_n)^2 + S_n{}^2)^{1/2}$ (44). The R_{ex}^{s+f} values at 3.5ppm for the three ω_1 values were obtained and fitted to Eq. (3) to obtain the amide f_s and k_{sw}, similar to that for processing the *in vivo* data. One hundred datasets were generated to determine the resulting variance in the fitted parameters.

The coupled Bloch equations can be written as $\frac{d\mathbf{M}}{dt} = \mathbf{AM} + \mathbf{M}_0$, where A is a 6 × 6 or 9 × 9 matrix for the two-pool model or the three-pool model, respectively. The water and solute pools each have three coupled equations representing their x, y, and z components. All numerical calculations of the CEST signals integrated the differential equations through the sequence using the ordinary differential equation solver (ODE45) in MATLAB 2018a (Math Works, Natick, MA, USA).

RESULTS

Fig. 1a and 1b illustrate the results of the two-pool model simulation, showing the simulated R_{ex}^{s} / ω_1^2 and R_{ex}^{f} / ω_1^2 values at 3.5ppm vs. ω_1, respectively. The figures demonstrate that R_{ex}^{s} / ω_1^2 decreases greatly with the increase in ω_1 values, while R_{ex}^{f} / ω_1^2 is roughly insensitive to ω_1 values. For instance, (R_{ex}^{s} / ω_1^2 with a ω_1 of 1μT (7.39×10^{-7}) is approximately 7 times that with a ω_1 of 3.6μT (1.02×10^{-7}). On the other hand, R_{ex}^{s} / ω_1^2 with a ω_1 of 1μT (4.00×10^{-7}) is roughly equal to that with a ω_1 of 3.6μT (4.01×10^{-7})). This simulation verifies the simplification presented in Eqs. (5)-(7).

Fig. 2a-2c show simulated CEST Z–spectra and corresponding reference spectra from two– and the three–pool model simulations at low ω_1 values of 0.25μT, 0.5 μT, and 1μT. It is evident from the figures that although APT has a narrow peak at 3.5ppm, the amine CEST signal is very broad which decreases the baseline in the CEST Z-spectrum and overlaps with APT. Fig. 2d shows the simulated CEST Z-spectra and reference spectra from the three-pool model simulation at a high ω_1 value of 3.6μT, where the APT peak becomes unclear compared to the more significant amine CEST effect. Fig. 2e shows

$R_{ex}^{s+f} / \omega_1^2$ spectra from the three-pool model simulation at low and high ω_1 values. It is evident that the broad baselines (0–2ppm, 4.5–5ppm) in these $R_{ex}^{s+f} / \omega_1^2$ spectra, which are from the fast exchange amine, acquired at the low and the high ω_1, respectively, overlap, suggesting that the subtraction of the two $R_{ex}^{s+f} / \omega_1^2$ spectra can remove the contribution from the fast exchange amine CEST effect. Fig. 2f-2h show R_{ex}^{s} and R_{ex}^{f} spectra from the three-pool model simulation using Eq. (8) and Eq. (9), respectively, as well as R_{ex}^{s} and R_{ex}^{f} spectra from the two-pool model simulation at low ω_1 values of 0.25μT, 0.5 μT, and 1μT, respectively. At 3.5ppm, the R_{ex}^{s} and R_{ex}^{f} values obtained using Eq. (8) and Eq. (9) ($R_{es}^{s} = 0.62\,\%\,s^{-1}$, $R_{ex}^{f} = 0.23\,\%\,s^{-1}$) are 93% and 127% of those from the two-pool model simulation ($R_{ex}^{s} = 0.67\,\%\,s^{-1}$, $R_{ex}^{f} = 0.18\,\%\,s^{-1}$), respectively, for the low ω_1 of 0.25μT. Similarly, the R_{ex}^{s} and R_{ex}^{f} values obtained using Eq. (8) and Eq. (9) ($R_{ex}^{s} = 2.02\,\%\,s^{-1}$, $R_{ex}^{f} = 0.90\,\%\,s^{-1}$) are 91% and 127% of those from the two-pool model simulation ($R_{ex}^{s} = 2.21\,\%\,s^{-1}$, $R_{ex}^{f} = 0.71\,\%\,s^{-1}$), respectively, for the low ω_1 of 0.5μT. Finally, the R_{ex}^{s} and R_{ex}^{f} values obtained using Eq. (8) and Eq. (9) ($R_{ex}^{s} = 4.56\,\%\,s^{-1}$, $R_{ex}^{f} = 3.60\,\%\,s^{-1}$) are 86% and 126% of those from the two-pool model simulation ($R_{ex}^{s} = 5.29\,\%\,s^{-1}$, $R_{ex}^{f} = 2.86\,\%\,s^{-1}$), respectively, for the low ω_1 of 1μT. This simulation indicates that our method using low and high power can approximately distinguish the contribution from the slow and fast exchange pool, albeit it underestimates APT and overestimates the fast exchange CEST effect.

Fig. 3a and 3b show the average of CEST Z–spectra measured from the whole brains of healthy rats, along with the corresponding reference Z–spectra obtained using EMR, for low ω_1 values of 0.25μT, 0.5μT, and 1μT, as well as a high ω_1 value of 3.6μT. Supporting information Figure S1 displays the residuals of the EMR fitting, and the relatively low RMS of the residuals suggests a high goodness of fit for the EMR. Supporting information Table S1 lists the fitted semi-solid MT parameters in the animal experiments. Fig. 3c presents the $R_{ex\_EMR}^{s+f} / \omega_1^2$ spectra from the measured CEST Z–spectra, using low ω_1 values of 0.25μT, 0.5μT, and 1μT, as well as a high ω_1 value 3.6μT. It is worth noting that the $R_{ex\_EMR}^{s+f} / \omega_1^2$ spectra obtained using the high ω_1 value is a sloping line, which is likely mainly from the fast exchange amine by comparison with the simulations in Fig. 2e. In contrast, the $R_{ex\_EMR}^{s+f} / \omega_1^2$ spectra obtained using the low ω_1 values should have contributions not only from the fast exchange amine CEST effect but also from the slow exchange APT effect. Additionally, there is a guanidinium proton CEST effect at 2ppm and a small CEST effect at 2.6ppm, which may arise from phosphocreatine (45,46). These overlapping CEST peaks also create a broad baseline, making it challenging to isolate the narrow APT peak from the fast exchange amine CEST peak based on their peak shapes. Fig. 3d displays the $R_{ex\_EMR}^{s}$ spectra calculated using Eq. (8) and the $R_{ex\_EMR}^{f}$ spectra using Eq. (9) from the measured CEST Z–spectra with the low ω_1 values of 0.25μT, 0.5μT, and 1μT, respectively. The $R_{ex\_EMR}^{f}$ values at 3.5ppm ($0.18\%s^{-1}$, $0.71\%s^{-1}$, $2.84\%s^{-1}$) are approximately 27%, 31%, and 65% of the $R_{ex\_EMR}^{s}$ values at 3.5ppm ($0.66\%s^{-1}$, $2.30\%s^{-1}$, $4.39\%s^{-1}$) for the low ω_1 values of 0.25μT, 0.5μT, and 1μT, respectively. Considering the estimation bias from the simulations in Fig. 2f-2h, the $R_{ex\_EMR}^{f}$ values at 3.5ppm ($0.18\%s^{-1}$/127%, $0.71\%s^{-1}$/127%, $2.84\%s^{-1}$/126%) should be approximately 20%, 22% , and 44% of the $R_{ex\_EMR}^{s}$ values at 3.5ppm ($0.66\%s^{-1}$/93%, $2.30\%s^{-1}$/91%, $4.39\%s^{-1}$/86%) for the low ω_1 values of 0.25μT,

0.5μT, and 1μT, respectively. Fig. 4 shows the plot $R^{s}_{ex\_EMR}$ and $R^{f}_{ex\_EMR}$ values at 3.5ppm obtained using Eq. (8) and Eq. (9) as well as their ratio vs. ω_1. It is important to note that $R^{f}_{ex\_EMR}$ increases exponentially with ω_1, while $R^{s}_{ex\_EMR}$ does not, resulting in an increase in their ratio as ω_1 increases.

Fig. 5a displays a plot of simulated R^{s+f}_{ex} values at 3.5ppm vs. ω_1 for six amine f_s values. It is notable that the R^{s+f}_{ex} value increases with amine f_s, especially at a higher ω_1. In Fig. 5b and 5c, the fitted amide f_s and amide k_{sw} values, respectively, are plotted against the six fast amine f_s values that were used to generate the simulated R^{s+f}_{ex} values at 3.5ppm. It can be observed that the fitted amide f_s and amide k_{sw} values increase with higher fast amine f_s values.

Fig. 6a, 6c, and 6e display the average of the measured CEST Z–spectra and the corresponding reference spectra obtained using the six–pool model fit of the APT effect, two–pool model fit of all CEST effects, and six–pool model fit with inclusion of all CEST effects, respectively, from tumors. Fig. 6b, 6d, and 6f illustrate the average of the measured CEST Z–spectra and the corresponding reference spectra obtained using the six–pool model fit of the APT effect, two–pool model fit of all CEST effect, six-pool model fit with inclusion of all CEST effect, respectively, from contralateral normal tissues. Supporting information Figure S2 and S3 show the fitted models and the residuals of the six-pool model and the two-pool model fit, respectively. The relatively low RMS of the residuals indicates a high goodness of these fitting methods. Fig. 6g and 6h show the R_{ex} spectra ($R_{ex\_mfit\_6pool\_APT}$, $R_{ex\_mfit\_2pool\_CEST}$, and $R_{ex\_mfit\_6pool\_CEST}$) with a ω_1 of 1μT using the three quantification methods from tumors and contralateral normal tissues, respectively. Note that the $R_{ex\_mfit\_6pool\_CEST}$(3.5ppm) value is the highest, followed by $R_{ex\_mfit\_2pool\_CEST}$(3.5ppm) and then $R_{ex\_mfit\_6pool\_APT}$(3.5ppm). This is consistent with simulations in Supporting Information Figure S4 (simulation parameters are shown in Supporting Information Table S2), which suggest that the six-pool model fit of the APT effect has little or no contamination from the fast exchange amine, that the two-pool model fit has some contribution from the fast exchange amine, and that the six-pool model fit with inclusion of all CEST effects has the maximum contamination from the fast exchange amine.

Fig. 7a-7c shows the mean and standard deviation of R_{ex} quantified by the three quantification methods at 3.5ppm. Note that $R_{ex\_mfit\_6pool\_APT}$(3.5ppm) and $R_{ex\_mfit\_2pool\_CEST}$(3.5ppm) showed no significant difference between tumors and contralateral normal tissues. This is consistent with our previous reports using the same multiple-pool Lorentzian fit (24) or a three–point fitting method (32), which have a minimum contribution from the fast exchange amine. In contrast, $R_{ex\_mfit\_6pool\_CEST}$(3.5ppm) showed a significant difference between tumors and contralateral normal tissues. This significant decrease in $R_{ex\_mfit\_6pool\_CEST}$(3.5ppm) in tumors is in agreement with our previous report in the quantification of the fast exchange amine CEST effect in tumors (47). Therefore, the significant difference between tumors and contralateral normal tissues in $R_{ex\_mfit\_6pool\_CEST}$(3.5ppm) is likely due to contamination from the fast exchange amine CEST effect but not APT.

Fig. 8a and 8b display the fitted amide f_s from the three quantifications in tumors and contralateral normal tissues, respectively. Fig. 8c and 8d show the fitted amide k_{sw} from the three quantifications in tumors and contralateral normal tissues, respectively. It is evident that the fitted f_s and k_{sw} increase with greater contamination from the fast exchange amine CEST effect.

DISCUSSION

In this paper, we have demonstrated the contribution of the fast exchange amine to CEST signals at 3.5ppm at low ω_1 values ranging from 0.25 μT to 1μT and its impact on the quantification of the APT effect and the associated exchange parameters. We have shown that the fast exchange amine CEST effect increases exponentially with ω_1, consistent with Eq. (4) when ω_1 in the denominator is ignored. At higher ω_1 values, the increase in the APT effect with ω_1 becomes slower which is in agreement with Eq. (3). Due to this different dependence on ω_1, the relative size of the fast exchange amine CEST effect to APT effect increases at higher ω_1 values. We have found that although this contribution from the fast exchange amine is relative small (~20% of the APT effect) at ω_1 values of 0.25μT and 0.5 μT, it cannot be ignored (~40% of the APT effect) at ω_1 of 1μT at 9.4T. Based on Eq. (3) and Eq. (4), this relative contribution would be even higher at lower fields since the frequency offset between the amide and the fast exchange amine is closer. Additionally, the guanidinium proton at 2ppm may also contribute to the CEST signal at 3.5ppm at lower fields. Our study is based on steady–state CEST imaging. In non–steady–state CEST imaging, the relative contribution from the fast exchange amine to CEST signals at 3.5ppm may be stronger since the slow exchange pool takes longer to reach the steady state compared to the fast exchange pool. Supporting Information Figure S5-S7 confirm that the relative contributions from the fast exchange amine to CEST signals at 3.5ppm with higher ω_1 and at lower fields are stronger and that non–steady–state acquisition (saturation time is 1s, 2s, and 5s) has nearly no changes. Supporting information discussion S1 estimated the fast exchange pool concentration and discussed its origin.

The presence of the fast exchange amine CEST effect may impact the specificity of some APT quantification methods. Therefore, in applications such as stroke where both the APT and the fast exchange amine CEST effects vary, it is important to carefully evaluate the specificity of these quantification methods. Recently, a consensus paper suggests the use of an asymmetric analysis of two CEST signals acquired at ±3.5ppm (MTR_{asym}) with ω_1 of 2μT to obtain an APT weighted imaging, termed ATP_w, in clinical human imaging at 3T MRI (48). Supporting Information Figure S5-S7 indicate that the asymmetric analysis can reduce the contribution from the fast exchange amine CEST effect since its peak is broad and may extend to the other side of the water peak, especially at 3T. Further studies are necessary to determine the relative contributions from the fast exchange amine CEST as well as the guanidinium proton CEST effect to the MTR_{asym} at 3.5ppm at 3T.

Currently, there are several methods available to quantify CEST exchange parameters, including the fitting of Bloch–McConnell equations (49-54), quantification of exchange rate using varying saturation power (QUESP)) or RF saturation time (QUEST) (55-58),

omega plot analysis (59-62), ratiometric analysis (63-65), MR fingerprinting CEST and deep learning-based approaches (14,15,46,66-69). However, to apply these methods to *in vivo* quantification, it is necessary to isolate the APT effect from the overlapping fast exchange amine CEST effect. This step was ignored in most of the previous quantifications. Our studies in Fig. 3 and Fig. 6 show that both the use of EMR and the fitting of background DS and MT as reference signals cannot remove the fast exchange amine CEST effect. In addition, although the multiple-pool Lorentzian fit with low ω_1 values can minimize the contribution from the fast exchange amine CEST effect, it does not work well at a higher ω_1 values, where the effect is more significant. This is because the fast exchange amine CEST peak is not a Lorentzian function due to the coalesce effect, and thus cannot be accurately modeled by the Lorentzian function (20,24,47). The relative contribution from the fast exchange amine to CEST signals at 3.5ppm depends on the sequence parameters and B_0. The presence of a fast exchange amine CEST effect at low ω_1 values may be one factor that causes the different fitted amide–water exchange parameters in previous reports. Strictly speaking, the slow exchange amide pool does not have a Lorentzian line shape according a previous definition of the exchange effect in the rotating frame (70). However, since the APT peak is narrow, it can be still approximated as a Lorentzian function.

In our previous publication (20), we utilized a similar quantification method with low and high saturation power which is intended to not only separate the CEST effects from the slow and fast exchange pools but recover the CEST peak line shape of the fast exchange pools. However, because of this, the fitted CEST peak is modulated by the solute resonance frequency offset, making it not straightforward to show the fitted CEST spectrum containing contributions from all pools. In this paper, we have slightly modified the previous method to directly demonstrate how the fast exchange amine CEST peak extends to the amide offset and how the APT, fast exchange amine CEST, phosphocreatine CEST, and guanidinium proton CEST effects sum up and contribute to the CEST Z-spectrum. Although various quantification methods including APT* (32,71), polynomial and Lorentzian line-shape fitting (PLOF) (19,72), average saturation efficiency filter (ASEF) (72,73), chemical exchange rotation transfer (45,74-76), and Amine-proton exchange (APEX) (77), have been developed to quantify the APT or fast exchange amine CEST effects, few methods are used to estimate the fast exchange amine CEST effect at the low saturation power (i.e., =<1μT). The multiple-pool Lorentzian fit can quantify the amine CEST effect at low saturation power, but it depends on the fitting models, as the six-pool model Lorentzian fit actually reflects the average contribution from the fast exchange amine, phosphocreatine, and guanidinium proton CEST effects. In Eq. (9) in this paper, we showed the relationship between two fast exchange amine CEST effects acquired at high and low saturation power. Based on this, we can estimate the fast exchange amine CEST effect at low saturation power using the measured fast exchange amine CEST effect at high saturation power. With this relationship, other quantification methods can be also utilized to evaluate the relative contributions from APT and the fast exchange amines.

Previous reports have described downfield aromatic NOE (78,79). Since the NOE coupling rate is usually slow, it does not affect our method for quantifying the fast exchange amine

CEST effect. However, it may lead to overestimation of the APT effect, which suggests that the relative size of the fast exchange amine CEST effect to APT effect could be even higher.

To obtain the background reference signal from MT and water saturation, we used EMR. Supporting information discussion S2 discussed the robustness of the EMR method. In supporting Information Figure S8, we calculated R_{ex}^{s} and R_{ex}^{f} spectra from a seven-pool model (amide at 3.5ppm, fast exchange amine at 3ppm, guanidinium proton at 2ppm, water, NOE at −1.6ppm, NOE at −3.5ppm, semi-solid MT) with S_{ref} from the EMR fitting. We also calculated R_{ex}^{s} and R_{ex}^{f} spectra from a three-pool model (amide + amine + water) with S_{ref} obtained using a single water pool model (as shown in Fig. 2f-2h). The R_{ex}^{s} and R_{ex}^{f} spectra from these two simulation models match well, indicating that the EMR fitting successfully remove the MT effect.

The AREX method was used to quantify the CEST effect, which requires high SNR signals for the inverse subtraction of reference and label signals. Monte Carlo simulations of R_{ex}^{s} and R_{ex}^{f} at 3.5ppm at various noise levels are presented in Supporting Information Figure S9, indicating that the estimation of R_{ex}^{s} at low ω_1 values of 0.25μT and 0.5μT requires high SNR signals. To ensure sufficient SNR in estimating R_{ex}^{s} and R_{ex}^{f} in Fig. 3 and Fig. 4, we averaged CEST signals from the whole brains of the five animals.

CONCLUSION

Our results demonstrate that the relative contribution of the fast exchange amine CEST effect relative to APT increases with higher ω_1. At 1μT (9.4T), the fast exchange amine CEST accounts for about 40% of the APT effect, indicating its significance. This contribution is expected to be even more substantial at lower fields, non–steady–state acquisitions, or higher ω_1 values. Accurate quantification of amide-water exchange parameters requires careful consideration of experimental design to minimize the impact of the fast exchange amine CEST effect.

Supplementary Material

Refer to Web version on PubMed Central for supplementary material.

Grant Sponsor:

R21 AR074261, R03 EB029078, R01 EB029443

REFERENCES

1. Zhou JY, van Zijl PCM. Chemical exchange saturation transfer imaging and spectroscopy. Prog Nucl Mag Res Sp 2006;48(2–3):109–136.
2. van Zijl PCM, Yadav NN. Chemical Exchange Saturation Transfer (CEST): What is in a Name and What Isn't? Magnetic Resonance In Medicine 2011;65(4):927–948. [PubMed: 21337419]
3. Kim J, Wu Y, Guo Y, Zheng H, Sun PZ. A review of optimization and quantification techniques for chemical exchange saturation transfer MRI toward sensitive in vivo imaging. Contrast media & molecular imaging 2015;10(3):163–178. [PubMed: 25641791]

4. Wu B, Warnock G, Zaiss M, Lin C, Chen M, Zhou Z, Mu L, Nanz D, Tuura R, Delso G. An overview of CEST MRI for non-MR physicists. Ejnmmi Phys 2016;3(1).
5. van Zijl PCM, Lam WW, Xu JD, Knutsson L, Stanisz GJ. Magnetization Transfer Contrast and Chemical Exchange Saturation Transfer MRI. Features and analysis of the field-dependent saturation spectrum. Neuroimage 2018;168:222–241. [PubMed: 28435103]
6. Zhou J, Payen JF, Wilson DA, Traystman RJ, van Zijl PC. Using the amide proton signals of intracellular proteins and peptides to detect pH effects in MRI. Nature medicine 2003;9(8):1085–1090.
7. Jiang SS, Eberhart CG, Zhang Y, Heo HY, Wen ZB, Blair L, Qin HM, Lim M, Quinones-Hinojosa A, Weingart JD, Barker PB, Pomper MG, Laterra J, van Zijl PCM, Blakeley JO, Zhou JY. Amide proton transfer-weighted magnetic resonance image-guided stereotactic biopsy in patients with newly diagnosed gliomas. Eur J Cancer 2017;83:9–18. [PubMed: 28704644]
8. Choi YS, Ahn SS, Lee SK, Chang JH, Kang SG, Kim SH, Zhou JY. Amide proton transfer imaging to discriminate between low- and high-grade gliomas: added value to apparent diffusion coefficient and relative cerebral blood volume. Eur Radiol 2017;27(8):3181–3189. [PubMed: 28116517]
9. Togao O, Hiwatashi A, Yamashita K, Kikuchi K, Keupp J, Yoshimoto K, Kuga D, Yoneyama M, Suzuki SO, Iwaki T, Takahashi M, Iihara K, Honda H. Grading diffuse gliomas without intense contrast enhancement by amide proton transfer MR imaging: comparisons with diffusion- and perfusion-weighted imaging. Eur Radiol 2017;27(2):578–588. [PubMed: 27003139]
10. Jiang SS, Eberhart CG, Lim M, Heo HY, Zhang Y, Blair L, Wen ZB, Holdhoff M, Lin D, Huang P, Qin HM, Quinones-Hinojosa A, Weingart JD, Barker PB, Pomper MG, Laterra J, van Zijl PCM, Blakeley JO, Zhou JY. Identifying Recurrent Malignant Glioma after Treatment Using Amide Proton Transfer-Weighted MR Imaging: A Validation Study with Image-Guided Stereotactic Biopsy. Clin Cancer Res 2019;25(2):552–561. [PubMed: 30366937]
11. Sun PZ, Zhou J, Sun W, Huang J, van Zijl PC. Detection of the ischemic penumbra using pH-weighted MRI. Journal of Cerebral Blood Flow & Metabolism 2007;27(6):1129–1136. [PubMed: 17133226]
12. Harston GW, Tee YK, Blockley N, Okell TW, Thandeswaran S, Shaya G, Sheerin F, Cellerini M, Payne S, Jezzard P, Chappell M, Kennedy J. Identifying the ischaemic penumbra using pH-weighted magnetic resonance imaging. Brain : a journal of neurology 2015;138(Pt 1):36–42. [PubMed: 25564491]
13. Heo HY, Zhang Y, Burton TM, Jiang SS, Zhao YS, van Zijl PCM, Leigh R, Zhou JY. Improving the detection sensitivity of pH-weighted amide proton transfer MRI in acute stroke patients using extrapolated semisolid magnetization transfer reference signals. Magnetic Resonance In Medicine 2017;78(3):871–880. [PubMed: 28639301]
14. Heo HY, Han Z, Jiang SS, Schar M, van Zijl PCM, Zhou JY. Quantifying amide proton exchange rate and concentration in chemical exchange saturation transfer imaging of the human brain. Neuroimage 2019;189:202–213. [PubMed: 30654175]
15. Cohen O, Huang SN, McMahon MT, Rosen MS, Farrar CT. Rapid and quantitative chemical exchange saturation transfer (CEST) imaging with magnetic resonance fingerprinting (MRF). Magnetic Resonance In Medicine 2018;80(6):2449–2463. [PubMed: 29756286]
16. Cai K, Haris M, Singh A, Kogan F, Greenberg JH, Hariharan H, Detre JA, Reddy R. Magnetic resonance imaging of glutamate. Nature medicine 2012;18(2):302–306.
17. Cui J, Zu ZL. Towards the molecular origin of glutamate CEST (GluCEST) imaging in rat brain. Magnetic Resonance In Medicine 2020;83(4):1405–1417. [PubMed: 31691367]
18. Zhang XY, Xie JP, Wang F, Lin EC, Xu JZ, Gochberg DF, Gore JC, Zu ZL. Assignment of the molecular origins of CEST signals at 2ppm in rat brain. Magnetic Resonance In Medicine 2017;78(3):881–887. [PubMed: 28653349]
19. Chen L, Zeng HF, Xu X, Yadav NN, Cai SH, Puts NA, Barker PB, Li T, Weiss RG, van Zijl PCM, Xu JD. Investigation of the contribution of total creatine to the CEST Z-spectrum of brain using a knockout mouse model. NMR in biomedicine 2017;30(12).
20. Zhang XY, Wang F, Xu JZ, Gochberg DF, Gore JC, Zu ZL. Increased CEST specificity for amide and fast-exchanging amine protons using exchange-dependent relaxation rate. NMR in biomedicine 2018;31(2).

21. Zaiss M, Zu ZL, Xu JZ, Schuenke P, Gochberg DF, Gore JC, Ladd ME, Bachert P. A combined analytical solution for chemical exchange saturation transfer and semi-solid magnetization transfer. NMR in biomedicine 2015;28(2):217–230. [PubMed: 25504828]
22. Zaiss M, Bachert P. Exchange-dependent relaxation in the rotating frame for slow and intermediate exchange - modeling off-resonant spin-lock and chemical exchange saturation transfer. NMR in biomedicine 2013;26(5):507–518. [PubMed: 23281186]
23. Zaiss M, Bachert P. Chemical exchange saturation transfer (CEST) and MR Z-spectroscopy in vivo: a review of theoretical approaches and methods. Physics in medicine and biology 2013;58(22):R221–269. [PubMed: 24201125]
24. Zhang XY, Wang F, Li H, Xu JZ, Gochberg DF, Gore JC, Zu ZL. Accuracy in the quantification of chemical exchange saturation transfer (CEST) and relayed nuclear Overhauser enhancement (rNOE) saturation transfer effects. NMR in biomedicine 2017;30(7).
25. Cai K, Haris M, Singh A, Kogan F, Greenberg JH, Hariharan H, Detre JA, Reddy R. Magnetic resonance imaging of glutamate. Nature medicine 2012;18(2):302–306.
26. Zaiss M, Xu J, Goerke S, Khan IS, Singer RJ, Gore JC, Gochberg DF, Bachert P. Inverse Z-spectrum analysis for spillover, MT-, and T1-corrected steady-state pulsed CEST-MRI-application to pH-weighted MRI of acute stroke. Nmr in Biomedicine 2014;27(3):240–252. [PubMed: 24395553]
27. Jones CK, Huang A, Xu JD, Edden RAE, Schar M, Hua J, Oskolkov N, Zaca D, Zhou JY, McMahon MT, Pillai JJ, van Zijl PCM. Nuclear Overhauser enhancement (NOE) imaging in the human brain at 7 T. Neuroimage 2013;77(0):114–124. [PubMed: 23567889]
28. Gochberg DF, Gore JC. Quantitative magnetization transfer imaging via selective inversion recovery with short repetition times. Magnetic Resonance In Medicine 2007;57(2):437–441. [PubMed: 17260381]
29. Heo HY, Zhang Y, Lee DH, Hong XH, Zhou JY. Quantitative Assessment of Amide Proton Transfer (APT) and Nuclear Overhauser Enhancement (NOE) Imaging with Extrapolated Semi-Solid Magnetization Transfer Reference (EMR) Signals: Application to a Rat Glioma Model at 4.7 Tesla. Magnetic Resonance in Medicine 2016;75(1):137–149. [PubMed: 25753614]
30. Heo HY, Zhang Y, Jiang SS, Lee DH, Zhou JY. Quantitative Assessment of Amide Proton Transfer (APT) and Nuclear Overhauser Enhancement (NOE) Imaging with Extrapolated Semisolid Magnetization Transfer Reference (EMR) Signals: II. Comparison of Three EMR Models and Application to Human Brain Glioma at 3 Tesla. Magnetic Resonance in Medicine 2016;75(4):1630–1639. [PubMed: 26033553]
31. Heo HY, Zhang Y, Burton TM, Jiang S, Zhao Y, Van Zijl PC, Leigh R, Zhou JY. Improving the Detection Sensitivity of pH-Weighted Amide Proton Transfer MRI in Acute Stroke Patients Using Extrapolated Semisolid Magnetization Transfer Reference Signals. Magnetic Resonance in Medicine 2017:DOI: 10.1002/mrm.26799.
32. Xu JZ, Zaiss M, Zu ZL, Li H, Xie JP, Gochberg DF, Bachert P, Gore JC. On the origins of chemical exchange saturation transfer (CEST) contrast in tumors at 9.4 T. NMR in biomedicine 2014;27(4):406–416. [PubMed: 24474497]
33. Zhang XY, Wang F, Afzal A, Xu JZ, Gore JC, Gochberg DF, Zu ZL. A new NOE-mediated MT signal at around-1.6 ppm for detecting ischemic stroke in rat brain. Magn Reson Imaging 2016;34(8):1100–1106. [PubMed: 27211260]
34. Zhang XY, Wang F, Jin T, Xu JZ, Xie JP, Gochberg DF, Gore JC, Zu ZL. MR imaging of a novel NOE-mediated magnetization transfer with water in rat brain at 9.4T. Magnetic Resonance In Medicine 2017;78(2):588–597. [PubMed: 27604612]
35. Zu ZL. Ratiometric NOE(−1.6) contrast in brain tumors. NMR in biomedicine 2018;31(12).
36. Zu ZL. Toward more reliable measurements of NOE effects in CEST spectra at around-1.6 ppm (NOE (−1.6)) in rat brain. Magnetic Resonance In Medicine 2019;81(1):208–219. [PubMed: 30058128]
37. Zu ZL, Lin EC, Louie EA, Xu JZ, Li H, Xie JP, Lankford CL, Chekmenev EY, Swanson SD, Does MD, Gore JC, Gochberg DF. Relayed nuclear Overhauser enhancement sensitivity to membrane Cho phospholipids. Magnetic Resonance In Medicine 2020.

38. Cui J, Zhao Y, Wang F, Gochberg DF, Zu ZL. Contribution of blood to nuclear Overhauser effect at-1.6 ppm. Magnetic Resonance In Medicine 2022;87(1):409–416. [PubMed: 34480767]
39. Heo HY, Jones CK, Hua J, Yadav N, Agarwal S, Zhou JY, van Zijl PCM, Pillai JJ. Whole-Brain Amide Proton Transfer (APT) and Nuclear Overhauser Enhancement (NOE) Imaging in Glioma Patients Using Low-Power Steady-State Pulsed Chemical Exchange Saturation Transfer (CEST) Imaging at 7T. Journal Of Magnetic Resonance Imaging 2016;44(1):41–50. [PubMed: 26663561]
40. Heo HY, Zhang Y, Jiang S, Lee DH, Zhou J. Quantitative assessment of amide proton transfer (APT) and nuclear overhauser enhancement (NOE) imaging with extrapolated semisolid magnetization transfer reference (EMR) signals: II. Comparison of three EMR models and application to human brain glioma at 3 Tesla. Magnetic Resonance in Medicine 2016;75(4):1630–1639. [PubMed: 26033553]
41. Wolff SD, Balaban RS. Magnetization Transfer Contrast (Mtc) and Tissue Water Proton Relaxation Invivo. Magnetic Resonance in Medicine 1989;10(1):135–144. [PubMed: 2547135]
42. Henkelman RM, Stanisz GJ, Graham SJ. Magnetization transfer in MRI: a review. NMR in biomedicine 2001;14(2):57–64. [PubMed: 11320533]
43. Windschuh J, Zaiss M, Meissner JE, Paech D, Radbruch A, Ladd ME, Bachert P. Correction of B1-inhomogeneities for relaxation-compensated CEST imaging at 7T. Nmr in Biomedicine 2015;28(5):529–537. [PubMed: 25788155]
44. Pierpaoli C, Basser PJ. Toward a quantitative assessment of diffusion anisotropy. Magnetic Resonance In Medicine 1996;36(6):893–906. [PubMed: 8946355]
45. Zu ZL, Louie EA, Lin EC, Jiang XY, Does MD, Gore JC, Gochberg DF. Chemical exchange rotation transfer imaging of intermediate-exchanging amines at 2 ppm. NMR in biomedicine 2017;30(10).
46. Chen L, Schar M, Chan KWY, Huang JP, Wei ZL, Lu HZ, Qin Q, Weiss RG, van Zijl PCM, Xu JD. In vivo imaging of phosphocreatine with artificial neural networks. Nat Commun 2020;11(1).
47. Zhang XY, Wang F, Li H, Xu JZ, Gochberg DF, Gore JC, Zu ZL. CEST imaging of fast exchanging amine pools with corrections for competing effects at 9.4 T. NMR in biomedicine 2017;30(7).
48. Zhou JY, Zaiss M, Knutsson L, Sun PZ, Ahn SS, Aime S, Bachert P, Blakeley JO, Cai KJ, Chappell MA, Chen M, Gochberg DF, Goerke S, Heo HY, Jiang SS, Jin T, Kim SG, Laterra J, Paech D, Pagel MD, Park JE, Reddy R, Sakata A, Sartoretti-Schefer S, Sherry AD, Smith SA, Stanisz GJ, Sundgren PC, Togao O, Vandsburger M, Wen ZB, Wu Y, Zhang Y, Zhu WZ, Zu ZL, van Zijl PCM. Review and consensus recommendations on clinical APT-weighted imaging approaches at 3T: Application to brain tumors. Magnetic Resonance In Medicine 2022;88(2):546–574. [PubMed: 35452155]
49. Sun PZ, van Zijl PC, Zhou J. Optimization of the irradiation power in chemical exchange dependent saturation transfer experiments. J Magn Reson 2005;175(2):193–200. [PubMed: 15893487]
50. Woessner DE, Zhang SR, Merritt ME, Sherry AD. Numerical solution of the Bloch equations provides insights into the optimum design of PARACEST agents for MRI. Magnetic Resonance in Medicine 2005;53(4):790–799. [PubMed: 15799055]
51. Li AX, Hudson RHE, Barrett JW, Jones CK, Pasternak SH, Bartha R. Four-Pool Modeling of Proton Exchange Processes in Biological Systems in the Presence of MRI-Paramagnetic Chemical Exchange Saturation Transfer (PARACEST) Agents. Magnetic Resonance In Medicine 2008;60(5):1197–1206. [PubMed: 18958857]
52. Sun PZ. Simplified and scalable numerical solution for describing multi-pool chemical exchange saturation transfer (CEST) MRI contrast. Journal Of Magnetic Resonance 2010;205(2):235–241. [PubMed: 20570196]
53. Murase K, Tanki N. Numerical solutions to the time-dependent Bloch equations revisited. Magn Reson Imaging 2011;29(1):126–131. [PubMed: 20832224]
54. Shah SM, Mougin OE, Carradus AJ, Geades N, Dury R, Morley W, Gowland PA. The z-spectrum from human blood at 7T. Neuroimage 2018;167:31–40. [PubMed: 29111410]
55. McMahon MT, Gilad AA, Zhou J, Sun PZ, Bulte JW, van Zijl PC. Quantifying exchange rates in chemical exchange saturation transfer agents using the saturation time and saturation power dependencies of the magnetization transfer effect on the magnetic resonance imaging signal

(QUEST and QUESP): Ph calibration for poly-L-lysine and a starburst dendrimer. Magnetic Resonance in Medicine 2006;55(4):836–847. [PubMed: 16506187]

56. Randtke EA, Chen LQ, Pagel MD. The reciprocal linear QUEST analysis method facilitates the measurements of chemical exchange rates with CEST MRI. Contrast media & molecular imaging 2014;9(3):252–258. [PubMed: 24700753]
57. Randtke EA, Chen LQ, Corrales LR, Pagel MD. The Hanes-Woolf Linear QUESP Method Improves the Measurements of Fast Chemical Exchange Rates with CEST MRI. Magnetic Resonance In Medicine 2014;71(4):1603–1612. [PubMed: 23780911]
58. Sun PZ. Simplified Quantification of Labile Proton Concentration-Weighted Chemical Exchange Rate (k(ws)) with RF Saturation Time Dependent Ratiometric Analysis (QUESTRA): Normalization of Relaxation and RF Irradiation Spillover Effects for Improved Quantitative Chemical Exchange Saturation Transfer (CEST) MRI. Magnetic Resonance In Medicine 2012;67(4):936–942. [PubMed: 21842497]
59. Dixon WT, Ren JM, Lubag AJM, Ratnakar J, Vinogradov E, Hancu I, Lenkinski RE, Sherry AD. A Concentration-Independent Method to Measure Exchange Rates in PARACEST Agents. Magnetic Resonance In Medicine 2010;63(3):625–632. [PubMed: 20187174]
60. Sun PZ, Wang Y, Dai Z, Xiao G, Wu R. Quantitative chemical exchange saturation transfer (qCEST) MRI – RF spillover effect-corrected omega plot for simultaneous determination of labile proton fraction ratio and exchange rate. Contrast media & molecular imaging 2014;9(4):268–275. [PubMed: 24706610]
61. Wu RH, Xiao G, Zhou IY, Ran CZ, Sun PZ. Quantitative chemical exchange saturation transfer (qCEST) MRI - omega plot analysis of RF-spillover-corrected inverse CEST ratio asymmetry for simultaneous determination of labile proton ratio and exchange rate. NMR in biomedicine 2015;28(3):376–383. [PubMed: 25615718]
62. Sun PZ. Quasi-steady-state CEST (QUASS CEST) solution improves the accuracy of CEST quantification: QUASS CEST MRI-based omega plot analysis. Magnetic Resonance In Medicine 2021;86(2):765–776. [PubMed: 33749052]
63. Ward KM, Balaban RS. Determination of pH using water protons and chemical exchange dependent saturation transfer (CEST). Magnetic Resonance In Medicine 2000;44(5):799–802. [PubMed: 11064415]
64. Moon BF, Jones KM, Chen LQ, Liu PL, Randtke EA, Howison CM, Pagel MD. A comparison of iopromide and iopamidol, two acidoCEST MRI contrast media that measure tumor extracellular pH. Contrast media & molecular imaging 2015;10(6):446–455. [PubMed: 26108564]
65. Longo DL, Dastru W, Digilio G, Keupp J, Langereis S, Lanzardo S, Prestigio S, Steinbach O, Terreno E, Uggeri F, Aime S. Iopamidol as a Responsive MRI-Chemical Exchange Saturation Transfer Contrast Agent for pH Mapping of Kidneys: In Vivo Studies in Mice at 7 T. Magnetic Resonance in Medicine 2011;65(1):202–211. [PubMed: 20949634]
66. Zhou ZW, Han P, Zhou B, Christodoulou AG, Shaw JL, Deng ZX, Li DB. Chemical exchange saturation transfer fingerprinting for exchange rate quantification. Magnetic Resonance In Medicine 2018;80(4):1352–1363. [PubMed: 29845651]
67. Kim B, Schar M, Park H, Heo HY. A deep learning approach for magnetization transfer contrast MR fingerprinting and chemical exchange saturation transfer imaging. Neuroimage 2020;221.
68. Perlman O, Zhu B, Zaiss M, Rosen MS, Farrar CT. An end-to-end AI-based framework for automated discovery of rapid CEST/MT MRI acquisition protocols and molecular parameter quantification (AutoCEST). Magnetic Resonance In Medicine 2022;87(6):2792–2810. [PubMed: 35092076]
69. Perlman O, Farrar CT, Heo HY. MR fingerprinting for semisolid magnetization transfer and chemical exchange saturation transfer quantification. NMR in biomedicine 2022.
70. Jin T, Autio J, Obata T, Kim S-G. Spin-locking versus chemical exchange saturation transfer MRI for investigating chemical exchange process between water and labile metabolite protons. Magn Reson Med 2011;65(5):1448–1460. [PubMed: 21500270]
71. Jin T, Wang P, Zong XP, Kim SG. MR imaging of the amide-proton transfer effect and the pH-insensitive nuclear overhauser effect at 9.4 T. Magnetic Resonance in Medicine 2013;69(3):760–770. [PubMed: 22577042]

72. Chen L, Barker PB, Weiss RG, van Zijl PCM, Xu JD. Creatine and phosphocreatine mapping of mouse skeletal muscle by a polynomial and Lorentzian line-shape fitting CEST method. Magnetic Resonance In Medicine 2019;81(1):69–78. [PubMed: 30246265]

73. Chung JJ, Jin T. Average saturation efficiency filter ASEF-CEST MRI of stroke rodents. Magnetic Resonance In Medicine 2023;89(2):565–576. [PubMed: 36300851]

74. Zu Z, Janve VA, Xu J, Does MD, Gore JC, Gochberg DF. A new method for detecting exchanging amide protons using chemical exchange rotation transfer. Magnetic Resonance in Medicine 2013;69(3):637–647. [PubMed: 22505325]

75. Zu ZL, Xu JZ, Li H, Chekmenev EY, Quarles CC, Does MD, Gore JC, Gochberg DF. Imaging Amide Proton Transfer and Nuclear Overhauser Enhancement Using Chemical Exchange Rotation Transfer (CERT). Magnetic Resonance In Medicine 2014;72(2):471–476. [PubMed: 24302497]

76. Zu Z, Lin EC, Louie EA, Jiang X, Lankford CL, Damon B, Does MD, Gore JC, Gochberg DF. Chemical exchange rotation transfer imaging of phosphocreatine in muscle. NMR in biomedicine 2020:e4437. [PubMed: 33283945]

77. Jin T, Wang P, Zong XP, Kim SG. Magnetic resonance imaging of the Amine-Proton EXchange (APEX) dependent contrast. Neuroimage 2012;59(2):1218–1227. [PubMed: 21871570]

78. Jin T, Kim SG. In vivo saturation transfer imaging of nuclear overhauser effect from aromatic and aliphatic protons: implication to APT quantification. Proceedings of International Society for Magnetic Resonance in Medicine 2013;Salt Lake City, Utah, USA:p 2528.

79. Jin T, Kim SG. Role of chemical exchange on the relayed nuclear Overhauser enhancement signal in saturation transfer MRI. Magnetic Resonance In Medicine 2022;87(1):365–376. [PubMed: 34382694]

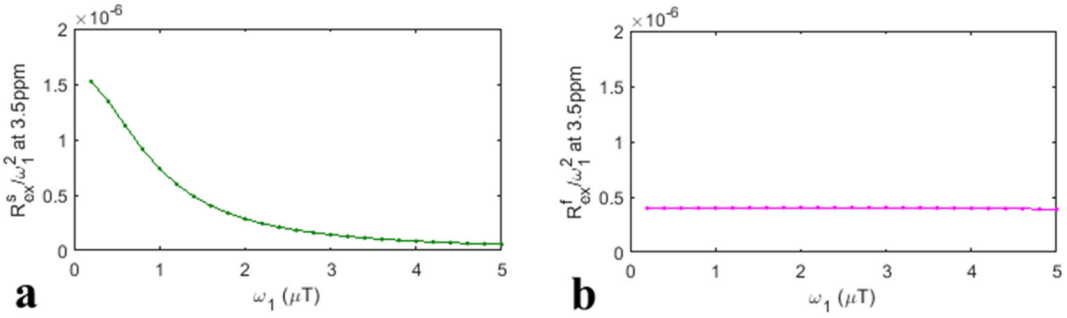

Fig 1.

Simulated R^s_{ex} / ω_1^2 (a) and R^f_{ex} / ω_1^2 (b) at 3.5ppm vs. ω_1 from the two-pool model simulation, where amide + water were used for the slow exchange effect and amine + water were used for the fast exchange effect.

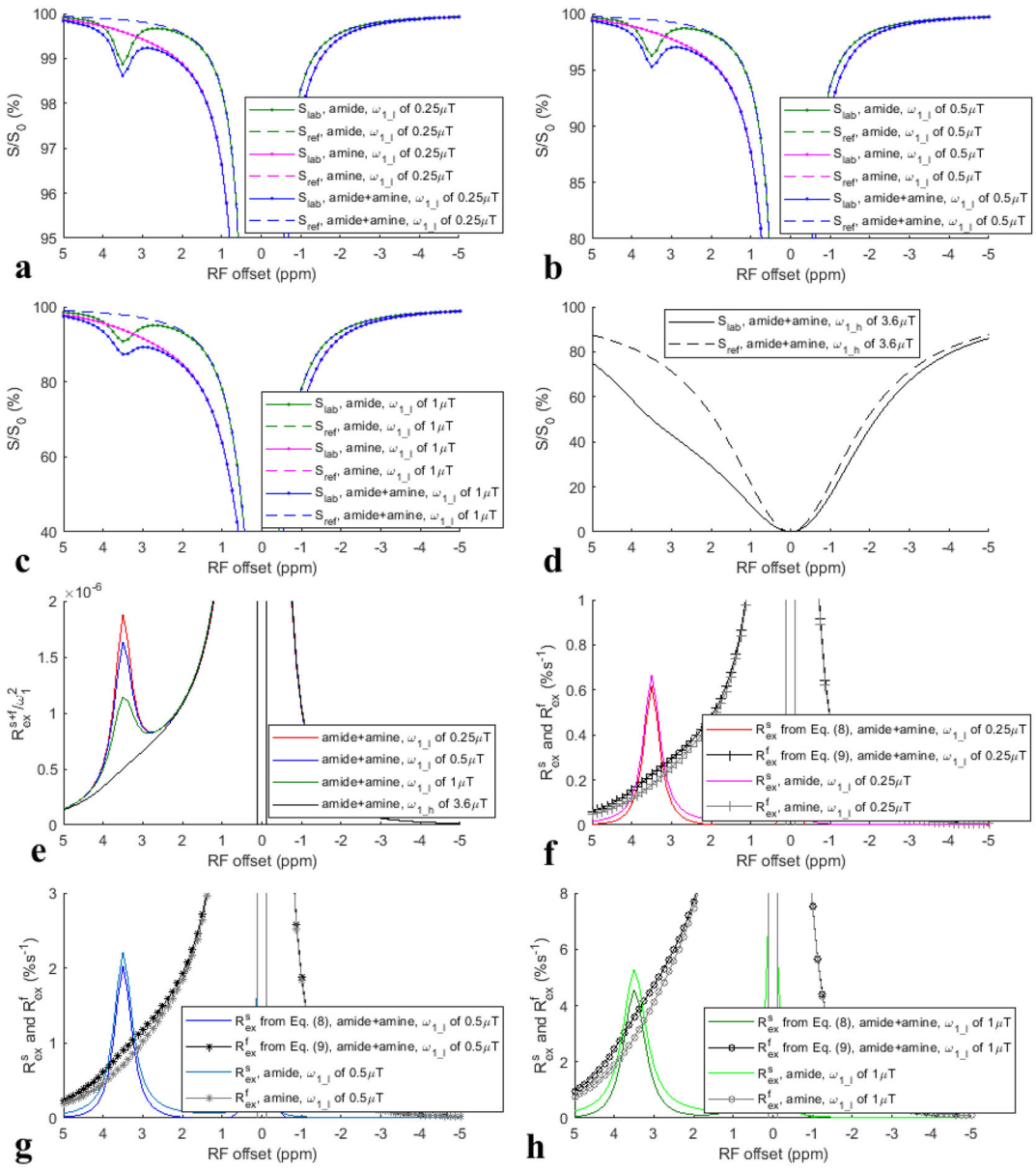

Fig 2.

CEST Z-spectra (S_{lab}) and the corresponding reference spectra (S_{ref}) from the two-pool (amide + water for the slow exchange effect, amine + water for the fast exchange effect) model and the three-pool (amide + amine + water) model simulation with low ω_1 values of 0.25μT, 0.5μT, and 1μT (a-c), as well as the three-pool model simulation with a high ω_1 value of 3.6μT (d). $R_{ex}^{s+f} / \omega_1^2$ spectra from the three-pool model simulation with ω_1 values of 0.25μT, 0.5μT, 1μT and 3.6μT (e). R_{ex}^{s} spectra using Eq. (8) and R_{ex}^{f} spectra using Eq. (9) from the three-pool model simulation with the low ω_1 values of 0.25μT, 0.5μT, and 1μT, respectively (f-h). R_{ex}^{s} and R_{ex}^{f} spectra from the two-pool model simulation with the low ω_1 values of 0.25μT, 0.5μT, and 1μT were also plotted in (f-h) for comparison with those from the three-pool model simulation. The three reference spectra (dashed lines) in (a-c) overlap.

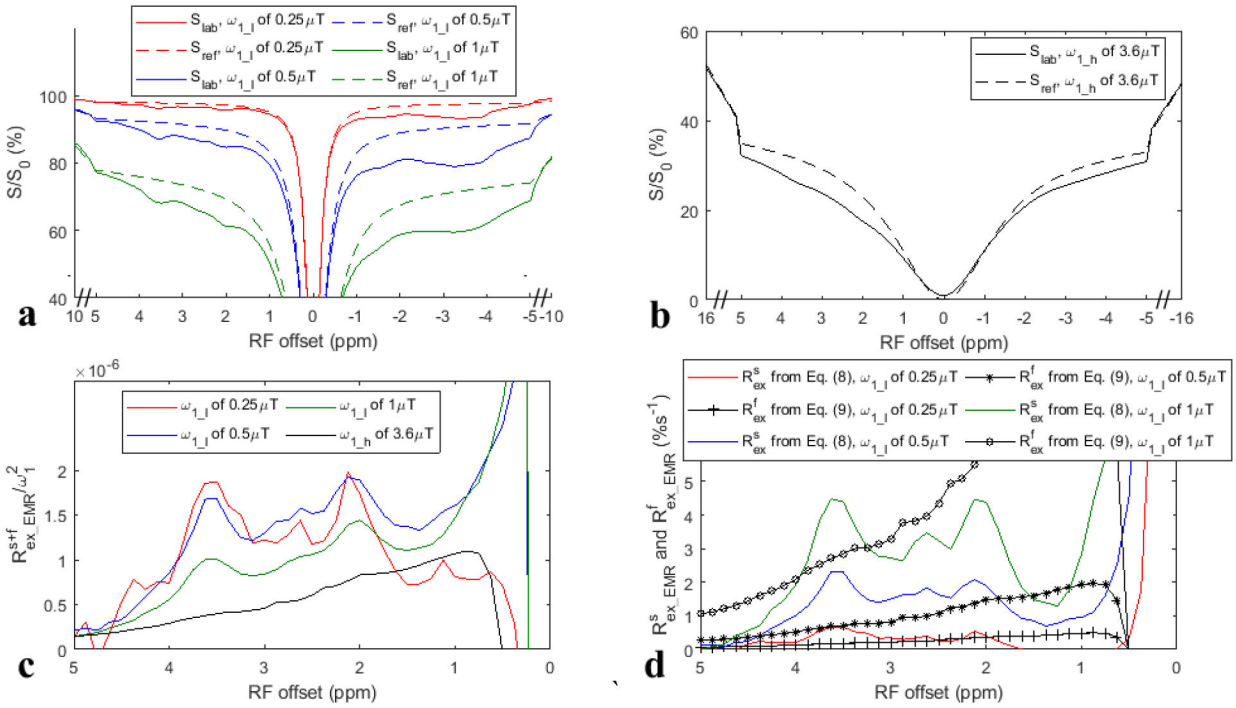

Fig. 3.

Averaged CEST Z-spectra from the whole brain (S_{lab}) and the corresponding EMR fitted reference spectrum (S_{ref}) acquired with low ω_1 values of 0.25μT, 0.5μT, and 1μT (a) as well as a high ω_1 value of 3.6uT (b). $R^{s+f}_{ex\_EMR} / \omega_1^2$ spectra with the low ω_1 values of 0.25μT, 0.5μT, and 1μT as well as the high ω_1 value of 3.6μT (c). $R^{s}_{ex\_EMR}$ and $R^{f}_{ex\_EMR}$ spectra obtained using Eq. (8) and Eq. (9) with the low ω_1 values of 0.25μT, 0.5μT, and 1μT, respectively (d).

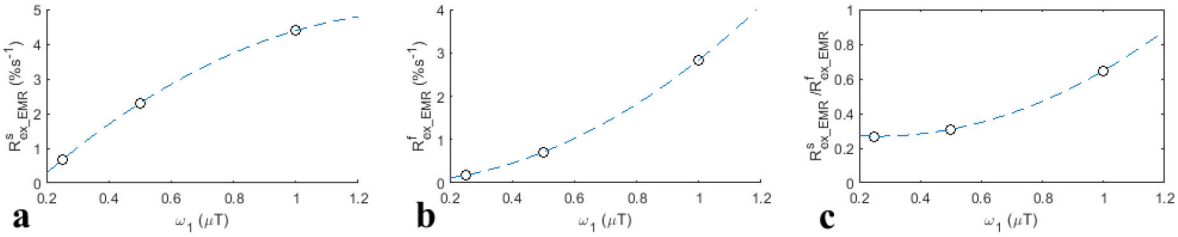

Fig. 4.

$R^s_{ex\_EMR}$ and $R^f_{ex\_EMR}$ values at 3.5ppm obtained using Eq. (8) and Eq. (9) (a, b) as well as their ratio (c) vs. ω_1 from the whole brain. Dashed lines are from the spline interpolation.

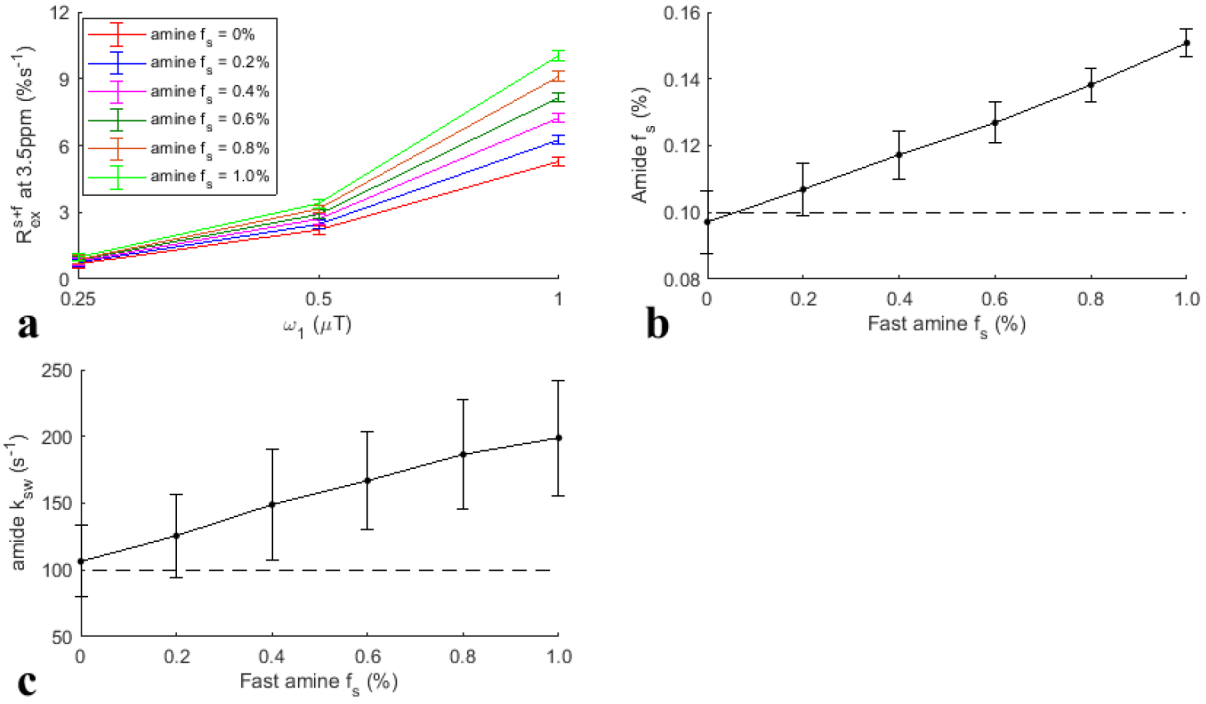

Fig. 5.

Simulated R_{ex}^{s+f} values at 3.5ppm vs. ω_1 for six fast exchange amine f_s values (a). Fitted amide f_s (b) and amide k_{sw} (c) vs. the six fast exchange amine f_s values from the simulated R_{ex}^{s+f} values at 3.5ppm. The dashed lines in (c) and (d) represent the ground truth values of the amide f_s (0.1%) and amide k_{sw} ($100s^{-1}$).

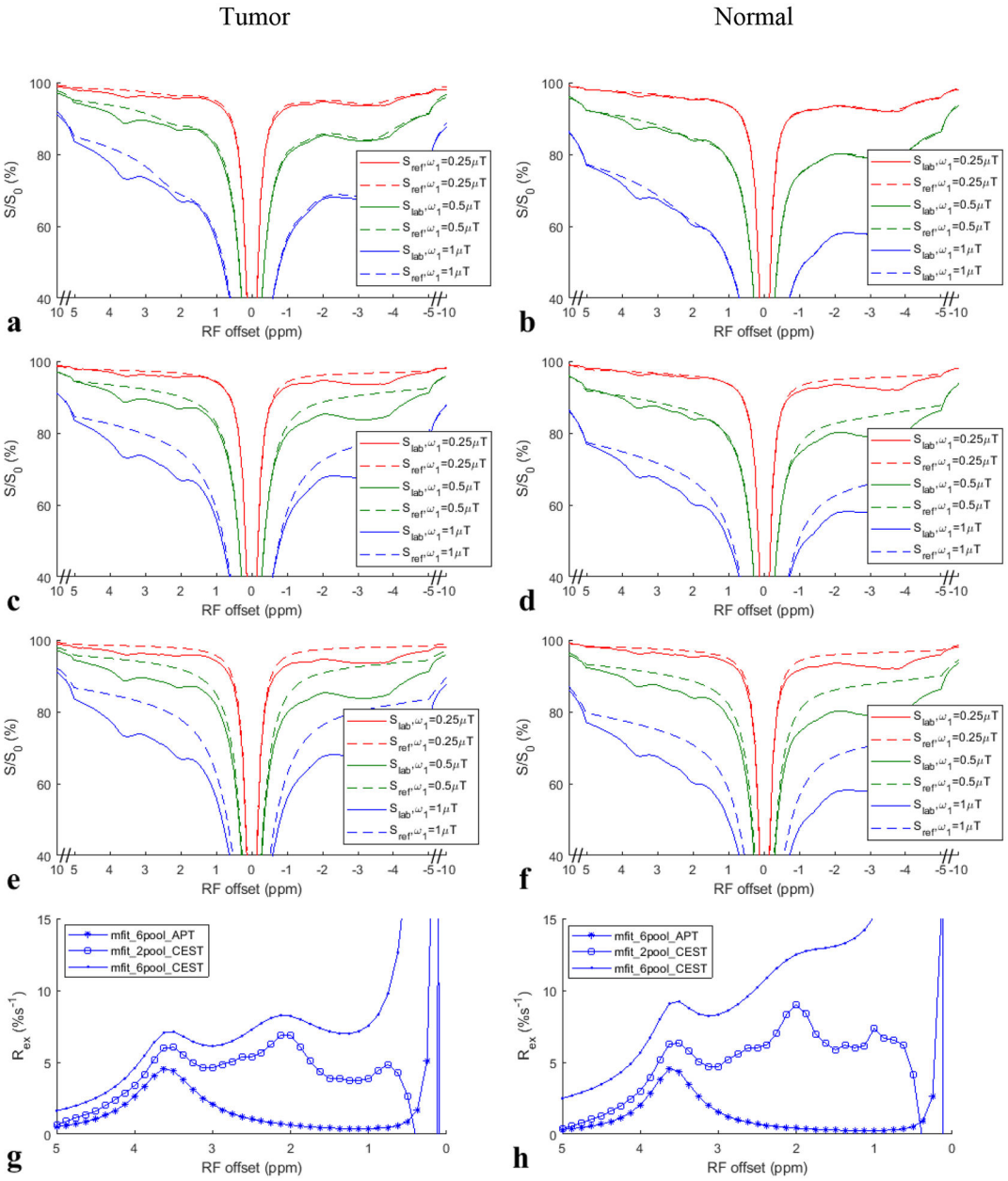

Fig. 6.

Average CEST Z-spectra and the corresponding reference spectra obtained using the six-pool model fit of APT effect (mfit_6pool_APT) (a, b), two-pool model fit of all CEST effect (mfit_2pool_CEST) (c, d), and six-pool model fit with inclusion of all CEST effect (mfit_6pool_CEST) (e, f), respectively, from tumors (left column) and contralateral normal tissues (right column). R_{ex} spectra with ω_1 of 1μT obtained using these three quantification methods from the tumors (g) and the contralateral normal tissues (h).

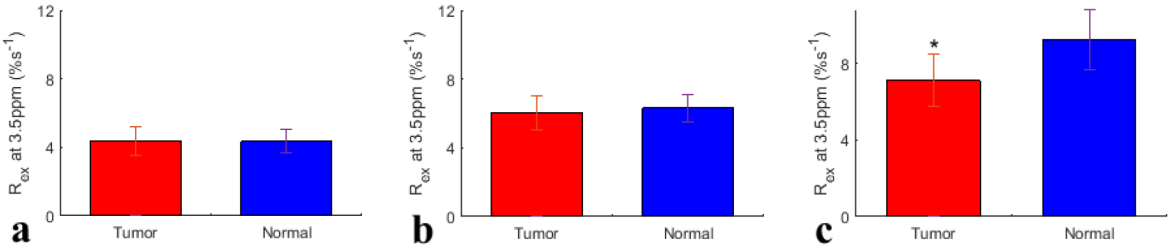

Fig. 7.

Mean and standard deviation of R_{ex} at 3.5ppm quantified by the six-pool model fit of APT effect (a), the two-pool model fit of all CEST effects (b), and the six-pool model fit with inclusion of all CEST effects (c), from tumors and contralateral normal tissues.

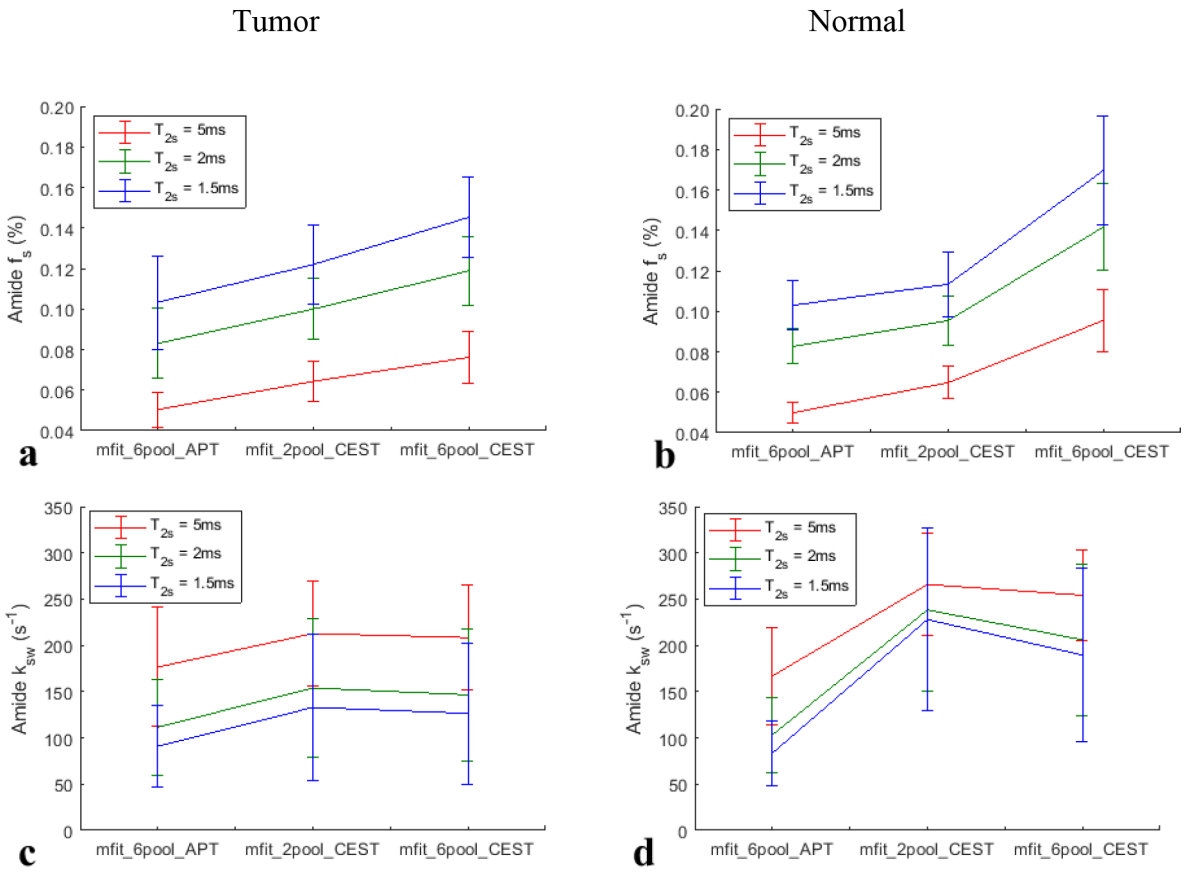

Fig. 8.

Fitted amide f_s (a, b) and amide k_{sw} (c, d) from the measured R_{ex} quantified using the six-pool model fit of APT effect (mfit_6pool_APT), two-pool model fit of all CEST effect (mfit_2pool_CEST), and six-pool model fit with inclusion of all CEST effect (mfit_6pool_CEST), respectively, from tumors (left column) and contralateral normal tissues (right column).

Table 1.

Starting points and boundaries of the amplitude (A), width (W), and offset (Δ) of all pools in the Lorentzian fit including the six-pool model and the two-pool model fit. The unit of peak width and offset is ppm.

	Start	Lower	Upper
A_{water}	0.9	0.02	1
W_{water}	1.4	0.1	10
Δ_{water}	0	−1	1
A_{amide}	0.025	0	0.2
W_{amide}	0.5	0.4	3
Δ_{amide}	3.5	3	4
A_{amine}	0.01	0	0.2
W_{amine}	1.5	0.5	5
Δ_{amine}	2	1	3
$A_{NOE(-1.6)}$	0.001	0	0.2
$W_{NOE(-1.6)}$	1	0	1.5
$\Delta_{NOE(-1.6)}$	−1.5	−2	−1
$A_{NOE(-3.5)}$	0.02	0	1
$W_{NOE(-3.5)}$	3	1	5
$\Delta_{NOE(-3.5)}$	−3.5	−4.5	−2.5
$A_{semi\text{-}solid\ MT}$	0.1	0	1
$W_{semi\text{-}solid\ MT}$	25	10	100
$\Delta_{semi\text{-}solid\ MT}$	0	−4	4

Table 2.

Sample parameters in the numerical simulations.

	water	**amide**	**fast amine at 3ppm**
f_s (%)	100	0.1	0, 0.2 0.4, 0.6, 0.8, 1.0
k_{sw} (s^{-1})	-	100	5000
T_1 (s)	1.5	1.5	1.5
T_2 (ms)	60	2	10
Δ (ppm)	0	3.5	3